Helheim velocity controlled both by terminus effects and subglacial hydrology in distinct realms of influence – Supplementary Information

A.N. Sommers[1], C.R. Meyer[1], K. Poinar[2], J. Mejia[2], M. Morlighem[1], H. Rajaram[3], K.L.P. Warburton[1], W. Chu[4]

[1]Dartmouth College, Hanover, NH, USA
[2]University at Buffalo, Buffalo, NY, USA
[3]Johns Hopkins University, Baltimore, MD, USA
[4]Georgia Institute of Technology, GA, USA

Supplement Contents

Table S1. Constants and parameter values used in this study

Symbol	Value	Units	Description
A	3.5×10^{-25}	$\mathrm{Pa}^{-3}\ \mathrm{s}^{-1}$	Flow law parameter (for ice at -10°C)
C	Spatially varying	$\mathrm{s}^{1/2}\ \mathrm{m}^{-1/2}$	Drag coefficient used in basal stress calculation
c_t	7.5×10^{-8}	$\mathrm{K\ Pa}^{-1}$	Change of pressure melting point with temperature
c_w	4.22×10^3	$\mathrm{J\ kg}^{-1}\ \mathrm{K}^{-1}$	Heat capacity of water
G	0.07	$\mathrm{W\ m}^{-2}$	Geothermal flux
g	9.81	$\mathrm{m\ s}^{-2}$	Gravitational acceleration
H	Varying	m	Ice thickness
L	3.34×10^5	$\mathrm{J\ kg}^{-1}$	Latent heat of fusion of water
n	3	Dimensionless	Flow law exponent
z_b	Varying	m	Bed elevation with respect to sea level
ν	1.787×10^{-6}	$\mathrm{m}^2\ \mathrm{s}^{-1}$	Kinematic viscosity of water
ω	0.001	Dimensionless	Parameter controlling nonlinear laminar/turbulent transition
ρ_i	917	$\mathrm{kg\ m}^{-3}$	Bulk density of ice
ρ_w	1000	$\mathrm{kg\ m}^{-3}$	Bulk density of water

Table S2. Summary of seasonal hydrology- and terminus-forced simulations with meltwater inputs to the bed in Region 1 and Region 2, firn aquifer inputs, and terminus forcing.

Simulation	Region 1	Region 2	Aquifer	Terminus
Seasonal	Transient	0	0	Free
Seasonal+firn aquifer	Transient	0	Steady	Free
Enhanced melt	Transient ×2	Transient ×2	Steady ×2	Free
Termforce	0	0	0	Prescribed velocity
Seasonal+termforce	Transient	0	0	Prescribed velocity
Seasonal+firn aquifer+termforce	Transient	0	Steady	Prescribed velocity
Enhanced melt+termforce	Transient ×2	Transient ×2	Steady ×2	Prescribed velocity

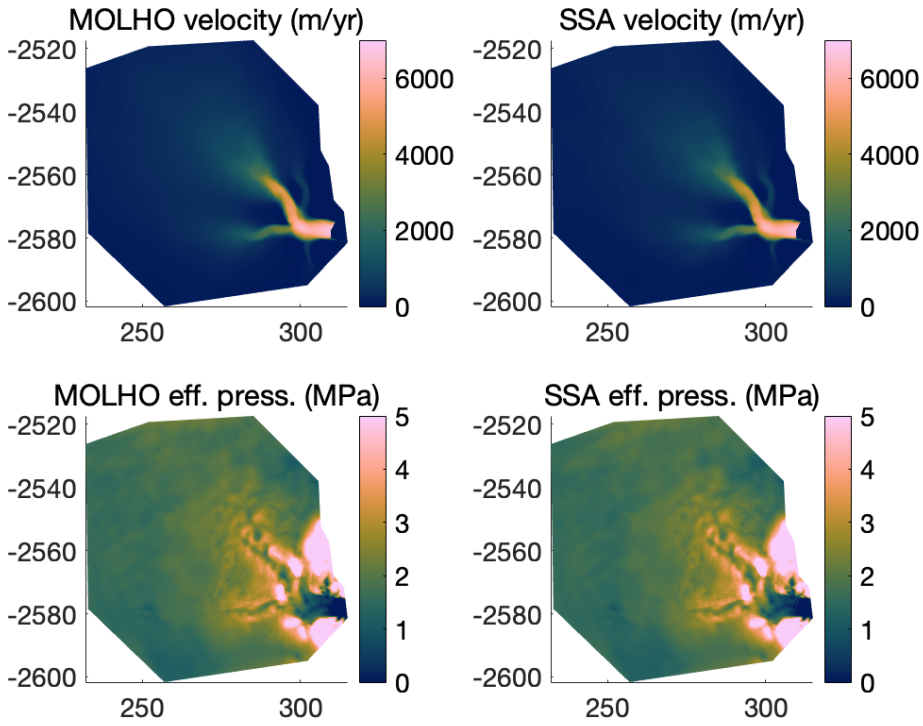

Figure S1. Winter base state ice velocity and effective pressure from SHAKTI-ISSM spin-up using MOLHO vs. SSA for ice dynamics calculations.

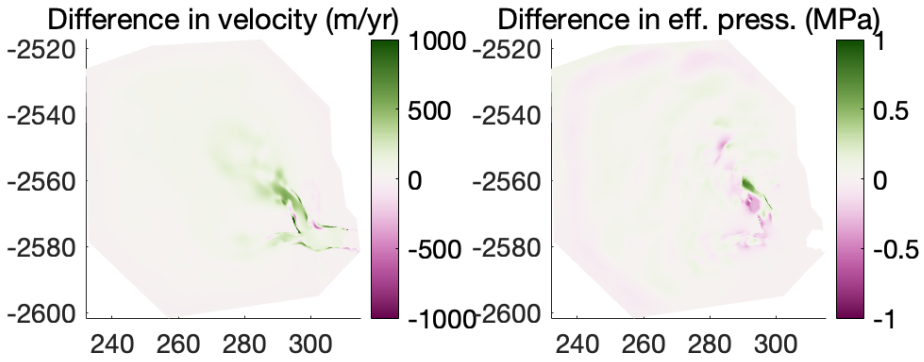

Figure S2. Difference in velocity and effective pressure from SHAKTI-ISSM spin-up using MOLHO vs. SSA for ice dynamics calculations.

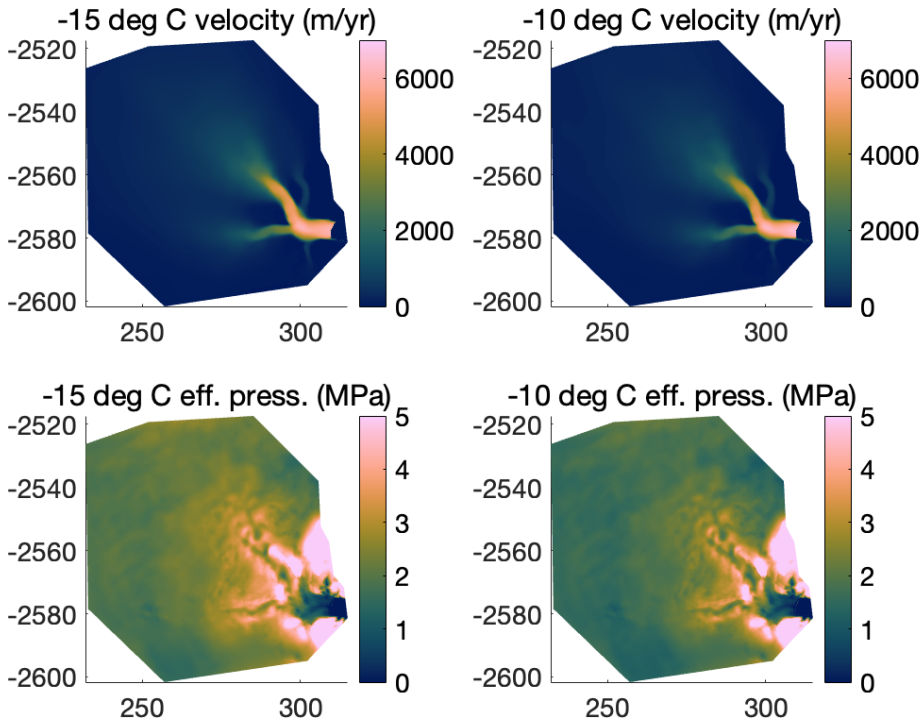

Figure S3. Winter base state ice velocity and effective pressure from SHAKTI-ISSM spin-up using a depth-integrated flow law parameter in SSA corresponding to -15^{o}C vs. -10^{o}C.

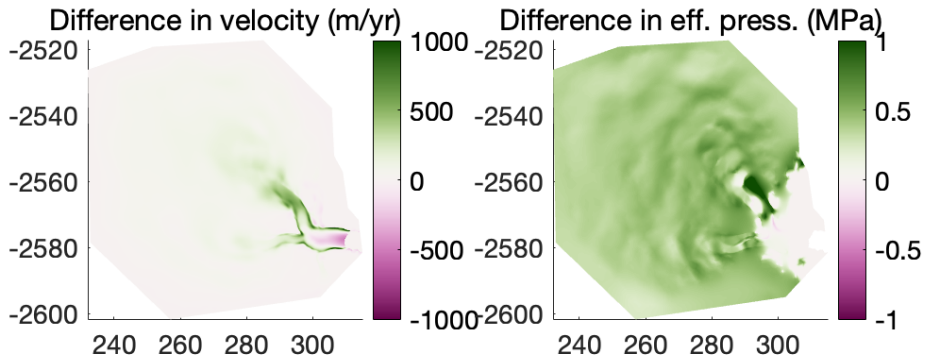

Figure S4. Difference in velocity and effective pressure between SHAKTI-ISSM spin-up using a depth-integrated flow law parameter in SSA corresponding to -15^{o}C vs. -10^{o}C.

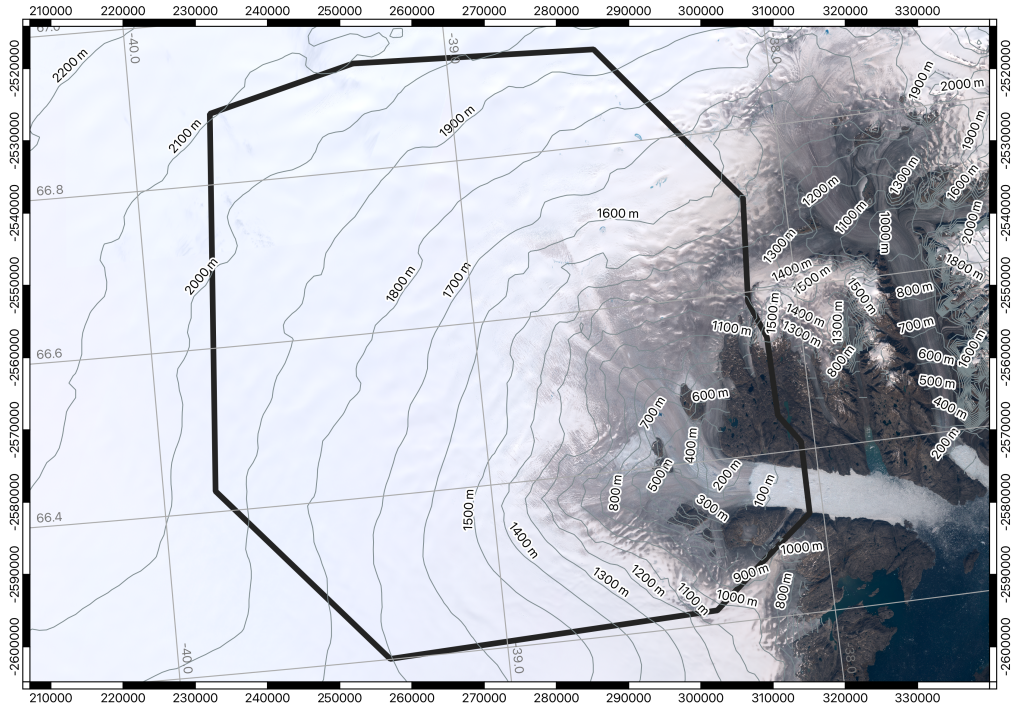

Figure S5. Model domain (black outline) overlaid on Sentinel-2 mosaic image of Helheim Glacier.

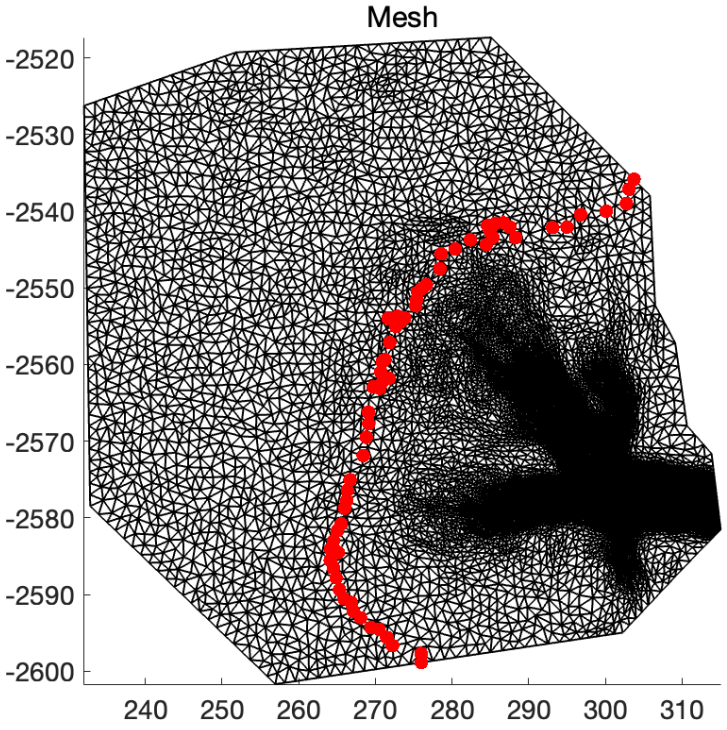

Figure S6. Unstructured triangular finite element mesh used in model simulations with firn aquifer drainage points (vertices with surface elevation 1500-1515 m) indicated by red dots.

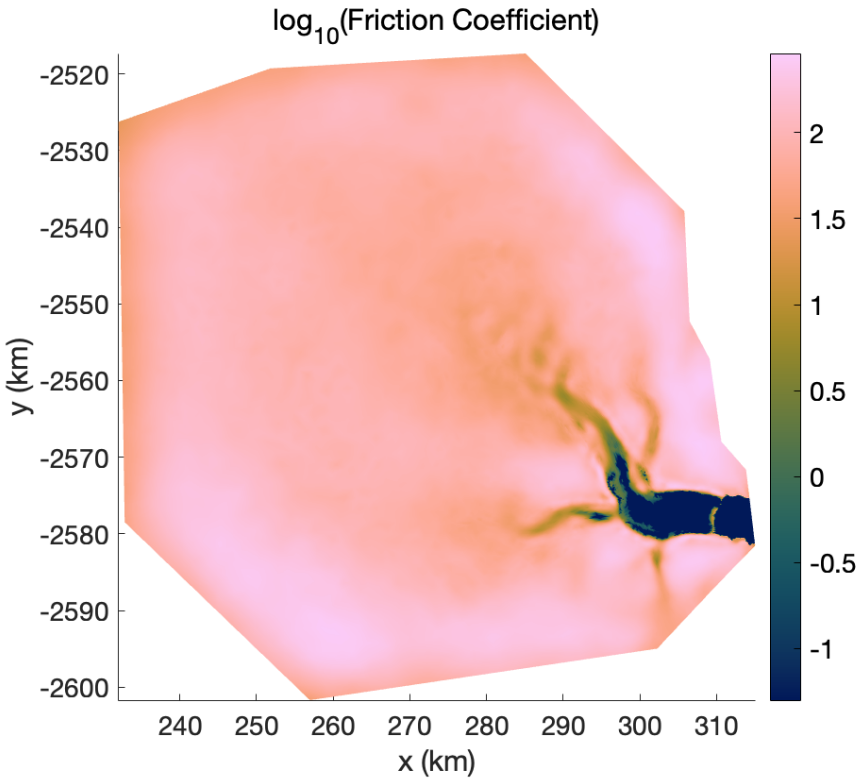

Figure S7. Friction coefficient (note the log scale) obtained used in transient through iterative spin-up inversion.

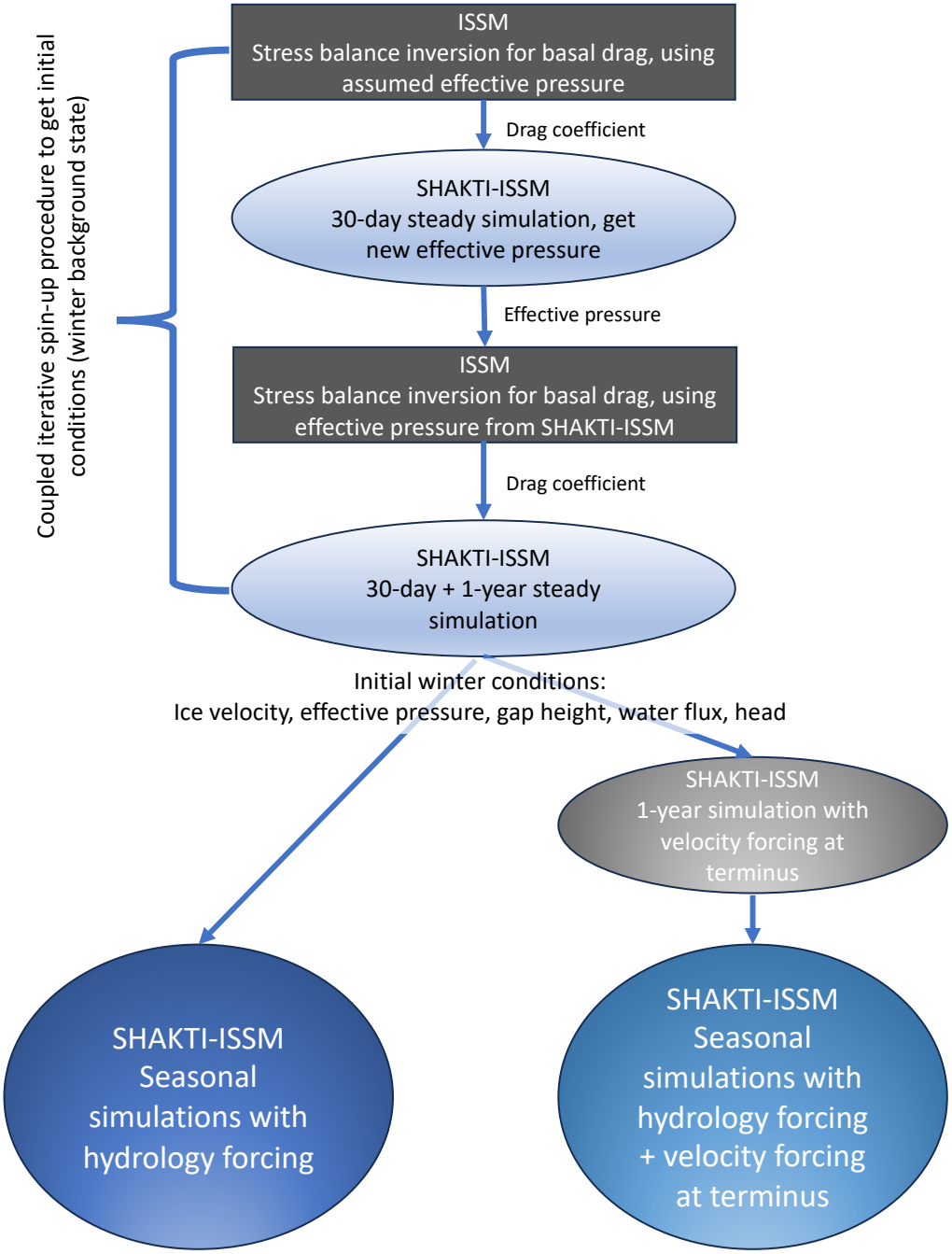

Figure S8. Schematic of SHAKTI-ISSM simulations, including iterative spin-up inversion for basal drag and effective pressure to generate initial winter base state.

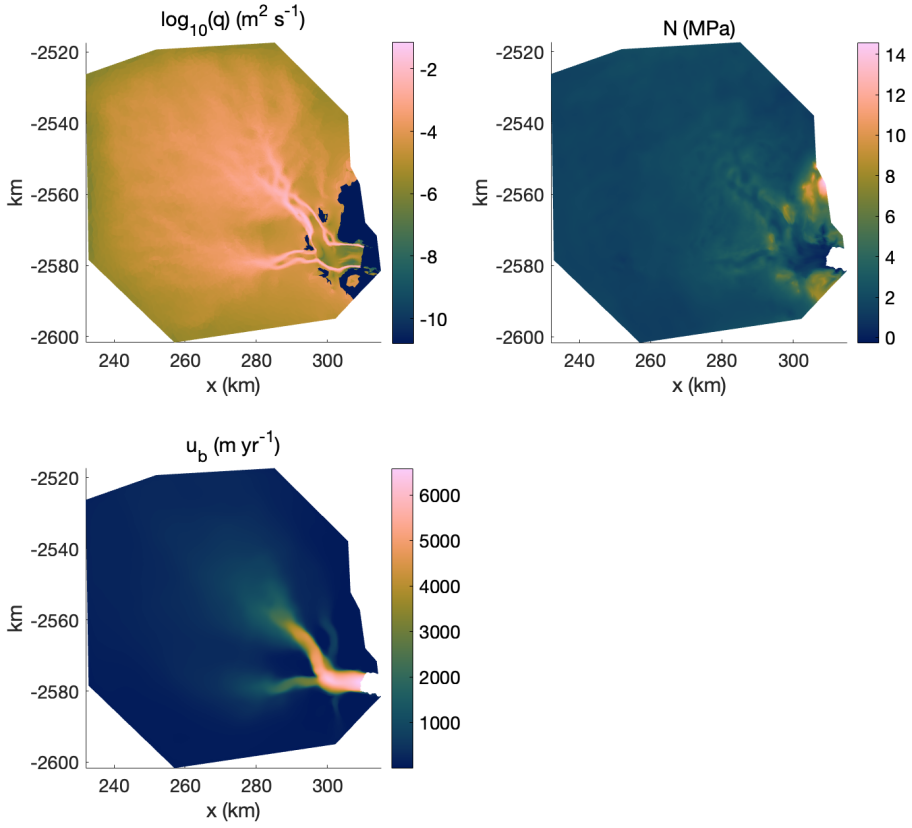

Figure S9. Winter state basal water flux ($\mathbf{q}$), effective pressure ($\mathbf{N}$), and ice sliding velocity $\mathbf{u_b}$ resulting from spin-up.

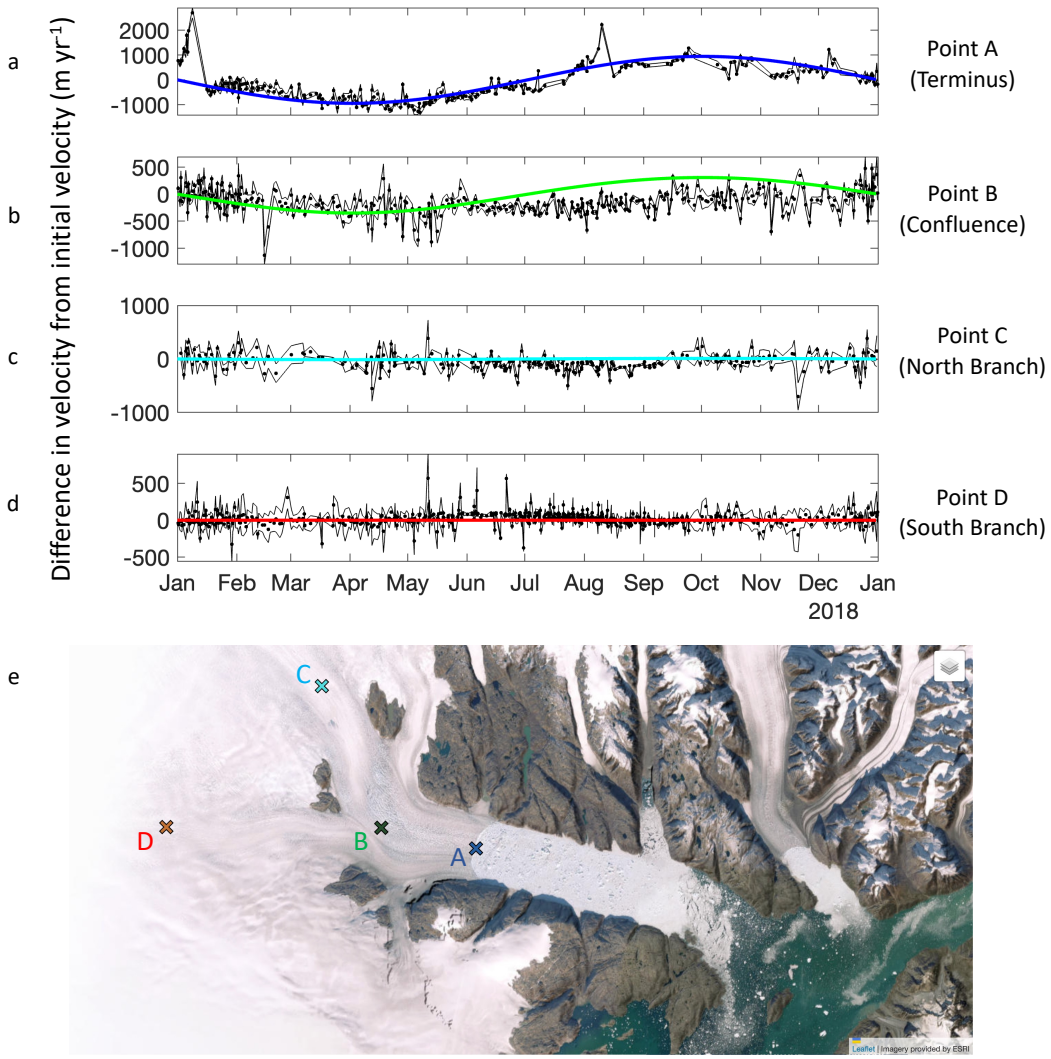

Figure S10. (a-d) Change in observed velocities relative to initial winter velocity (dots; observations from ITS_LIVE) with reported error (black lines) and modeled velocities (colored lines) from the *termforce+seasonal* simulation. (e) Location of points A-D overlaid on satellite image.

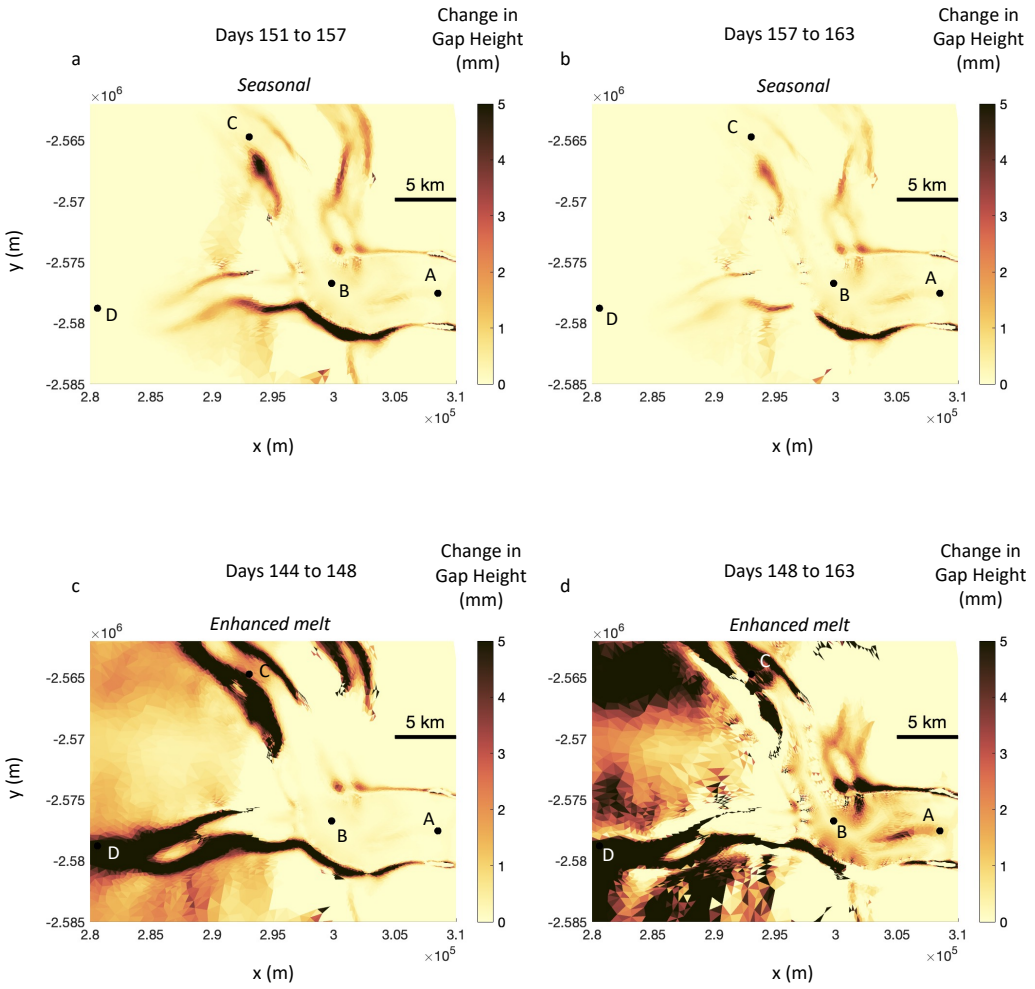

Figure S11. (a) Change in subglacial gap height in *seasonal* simulation between days 151 (minimum effective pressure at the confluence) and 157 (peak velocity at the confluence). (b) Change in subglacial gap height in *seasonal* simulation between days 157 (peak velocity at the confluence) and 163 (peak meltwater input). (c) Change in subglacial gap height in *enhanced melt* simulation between days 144 (peak velocity at the confluence) and 148 (minimum effective pressure at the confluence). (d) Change in subglacial gap height in *enhanced melt* simulation between days 148 (minimum effective pressure at the confluence) and 163 (peak meltwater input).

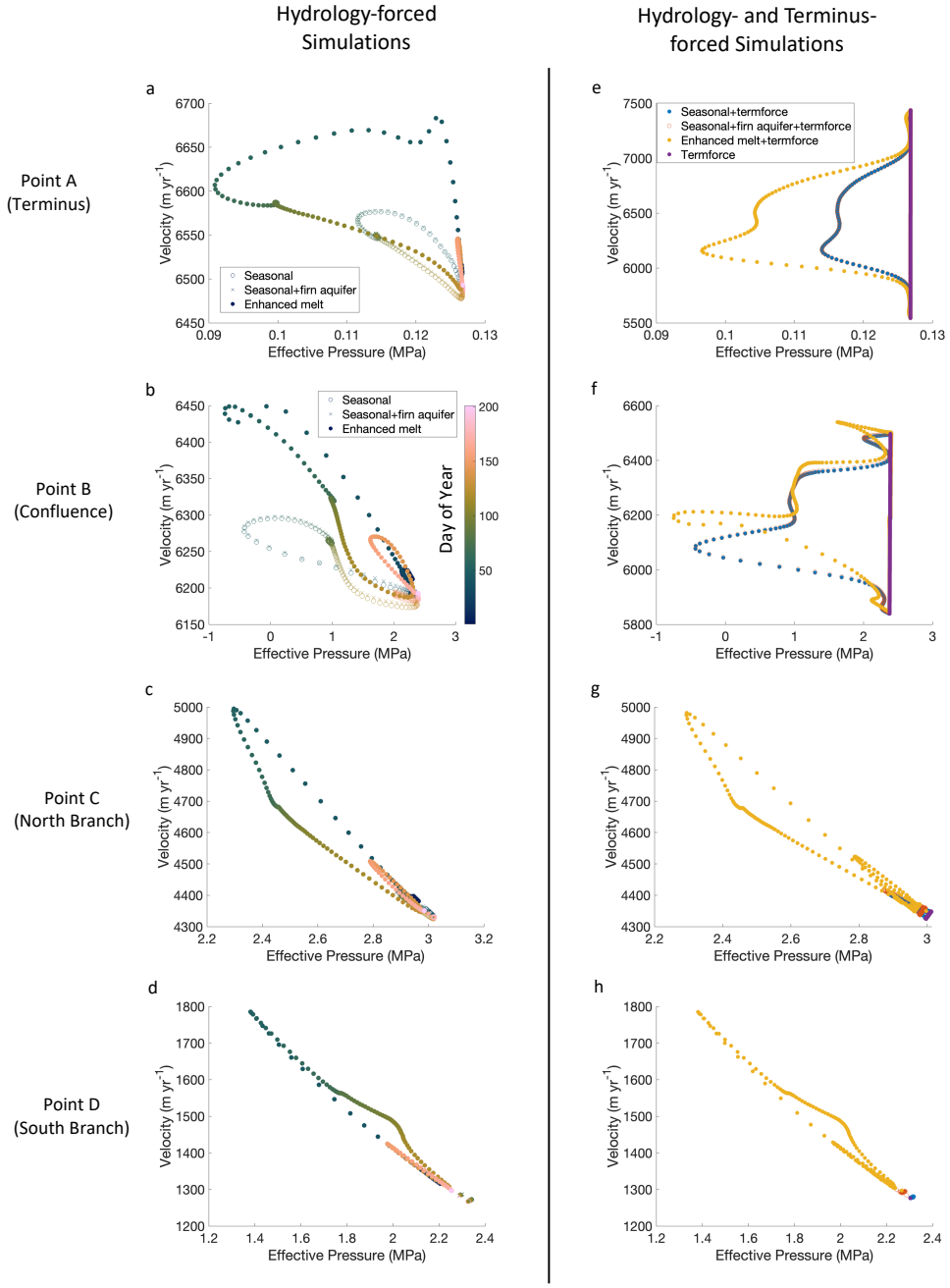

Figure S12. Velocity vs. effective pressure hysteresis loops for simulations forced by (a)-(d) meltwater inputs and (e)-(h) both meltwater inputs and terminus forcing.

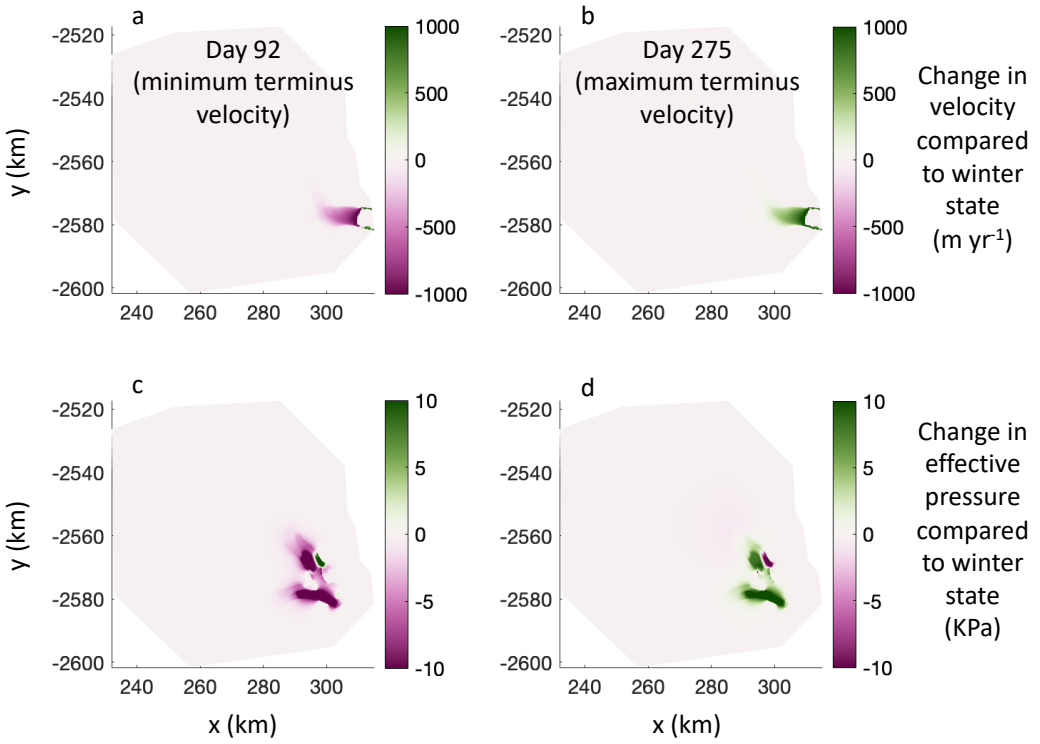

Figure S13. Change in sliding velocity relative to winter state in *termforce* simulation on April 2 and October 2, days of minimum (a) and maximum (b) forced terminus velocity. Change in effective pressure relative to winter state due to minimum (c) and maximum (d) terminus velocity forcing.

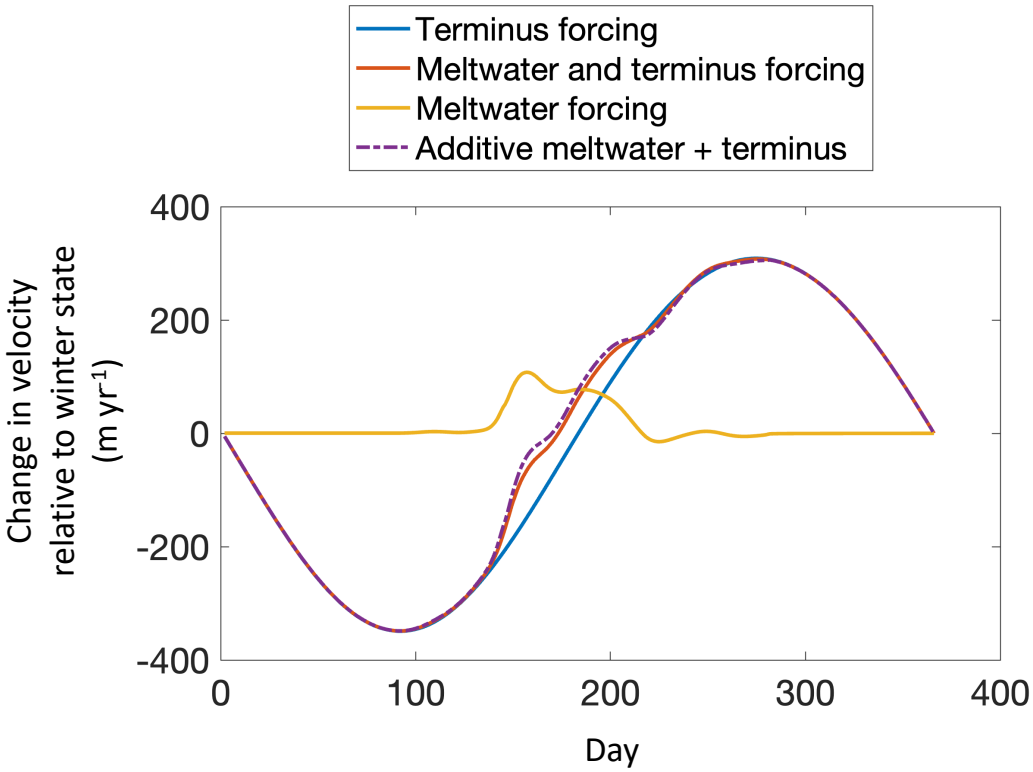

Figure S14. Change in velocity relative to winter state at point B (confluence) in seasonal simulations forced by meltwater only, terminus forcing only, meltwater and terminus forcing, compared to the additive velocity effects of meltwater- and terminus-forced simulations.